Electrically tuneable exciton-polaritons through free electron doping in monolayer WS_2 microcavities

*Henry A. Fernandez, Freddie Withers, Saverio Russo, and William L. Barnes**

H. A. Fernandez, Dr. F. Withers, Prof. S. Russo, Prof. W. L. Barnes

Department of Physics and Astronomy, University of Exeter, EX4 4QL, United Kingdom

E-mail: W.L.Barnes@exeter.ac.uk

Keywords: exciton-polaritons, Rabi splitting, microcavity, 2D semiconductor, field effect transistor

We demonstrate control over light-matter coupling at room temperature combining a field effect transistor (FET) with a tuneable optical microcavity. Our microcavity FET comprises a monolayer tungsten disulfide WS_2 semiconductor which was transferred onto a hexagonal boron nitride flake that acts as a dielectric spacer in the microcavity, and as an electric insulator in the FET. In our tuneable system, strong coupling between excitons in the monolayer WS_2 and cavity photons can be tuned by controlling the cavity length, which we achieved with excellent stability, allowing us to choose from the second to the fifth order of the cavity modes. Once we achieve the strong coupling regime, we then modify the oscillator strength of excitons in the semiconductor material by modifying the free electron carrier density in the conduction band of the WS_2. This enables strong Coulomb repulsion between free electrons, which reduces the oscillator strength of excitons until the Rabi splitting completely disappears. We controlled the charge carrier density from 0 up to 3.2×10^{12} cm^{-2}, and over this range the Rabi splitting varies from a maximum value that depends on the cavity mode chosen, down to zero, so the system spans the strong to weak coupling regimes.

1. Introduction

Exciton-polaritons are hybrid bosonic quasiparticles that have properties of both of their constituents: material properties of excitons, responsible for strong non-linear interactions, and optical properties of photons, that make them low mass compared with bare excitons. These quasiparticles have enabled the observation of cold atom physics including Bose-Einstein condensation on a chip,[1] superfluidity,[2–4] and topological polaritons.[5] At the same time, owing to their hybrid light-matter nature, exciton-polaritons may provide the strong non-linearities needed to deliver the strongly interacting photons[6] sought by quantum technologies.[7] This scenario could be significantly enriched by the ability of novel quantum materials to support room temperature operation of exciton-polaritons and the addition of unique functionalities, such as on-chip tuneable strength of light-matter interactions. Atomically thin semiconductors, part of the family of transition metal dichalcogenides (TMDs), exhibit a range of unique optical properties, which makes them one of the most promising material systems for enabling quantum photonics.[8] Prominent optical transitions in TMDs are widely dominated by excitons with a surprisingly large binding energy[9] making them viable for room temperature quantum electrodynamics. Additionally, due to their large exciton oscillator strengths, TMDs support strong light-matter interactions even in their atomically thin form.[10–15] However, the tuneability of light-matter interactions in TMD-based devices, which would enable further control over non-linear interactions, is still in its infancy and further development is needed. To investigate both tuneability and control over the light-matter coupling of exciton-polaritons we designed[16] and fabricated tuneable Fabry-Pérot microcavities with a TMD-based transistor embedded within the microcavity. We chose the TMD material tungsten disulfide, WS_2, which exhibits the largest oscillator strength and the smallest damping factor among TMDs of chemical composition MX_2 (M = W, Mo; X = S, Se).[17] These properties make WS_2 the optimal semiconductor TMD for strong coupling

measurements of exciton-polaritons at visible frequencies, at room temperature, and in microcavities of moderate quality factor, Q ≈ 100. In our device, we increase the free carrier density of a WS_2 monolayer, which produces strong Coulomb screening of the free electrons that populate the conduction band.[18] This screening reduces the oscillator strength of neutral excitons, which therefore weakens the coupling strength of exciton-polaritons.[19] Electrical control of light-matter coupling has been demonstrated in a monolithic microcavity filled with carbon nanotubes,[20] where near infrared excitons were strongly coupled to a single microcavity mode. By applying a range of gate voltages, the system was observed to cross reversibly from the weak to the strong coupling regime. Recently, this phenomenon was observed in the visible range using a monolithic TMD microcavity,[21] showing similar results. In our study we significantly extend the work by applying gate voltages sufficient to reach the saturation regime of the light-matter coupling strength, characterized by the vacuum Rabi splitting. For sufficiently negative values of the gate voltage, the Rabi splitting saturates to its maximum value, whilst for sufficiently positive values of the gate voltage (high electron carrier density), the Rabi splitting was completely eliminated. These observations allow us to explain the functional dependence of the Rabi splitting on the gate voltage and to probe the nature of the Coulomb screening process. In this report we studied a WS_2 microcavity in which the TMD excitons are strongly coupled to microcavity modes that can be chosen from the third-order to the fifth-order by controlling the cavity length in a tuneable way. We observed a dependence of the Rabi splitting on the electrically-controlled density of free electrons, a density that ranges from 0 up to 3×10^{12} cm^{-2}. Over this range the Rabi splitting varies from a maximum value (which depends on the order of the chosen cavity mode) down to zero, so that the hybrid system spans the strong to weak coupling regimes.

2. Results

2.1. WS_2-based field effect transistor

We first studied the WS_2-based field effect transistor without a microcavity. The transistor consisted of a Van der Waals heterostructure composed of WS_2 placed on top of a hexagonal boron nitride (hBN) flake (see experimental section for device fabrication details). The WS_2/hBN heterostructure was placed on a silver (Ag) film, which acts as a microcavity mirror (bottom mirror) as well as the gate contact of the transistor while WS_2 was kept as a ground contact (see Figure 1(a) and (b)). The hBN flake plays an important role in both the optical and the electronic performance of the transistor. For the optics, hBN acts as a dielectric spacer; the thickness of hBN determines the position at which the WS_2 flake is placed in the microcavity, and therefore the confined field intensity with which TMD excitons interact (see supporting information Figure S1). For the electronics, hBN acts as a dielectric insulator (∼3−4),[22] which prevents electrons from leaking between the WS_2 and the Ag gate electrode. Transmission measurements were performed through this device and we studied the evolution of the minimum in transmission associated with the WS_2 exciton for different values of the gate voltage. Figure 1(a) shows a microscope image of the top view of the WS_2 transistor; colored lines are drawn to indicate the edges of the different materials of the heterostructure, red for WS_2 and blue for hBN. The spot size for light collection (diameter 10 μm) is also indicated on the figure. The area of interest is a monolayer of WS_2 (1L-WS_2) electrically in contact with a multilayer flake (see Figure 1(a)) allowing for a minimized contact barrier height between the monolayer and multilayer TMD. The gate voltage is applied to the bottom Ag electrode while keeping the WS_2 electrode grounded. In this configuration, the application of a positive voltage between the two electrodes increases the carrier density of free charge carriers that populate the conduction band of the WS_2 monolayer, while the application of a negative voltage removes any doping of free charge carriers, leaving the sample electrically neutral in the range of

negative voltages applied. Because of the n-type character of WS_2, hole doping was not possible in the range of negative gate voltages. In Figure 1(b) a schematic side view of the sample is shown, in which the direction of propagation of the transmitted light is indicated by arrows and the position of the electrical contacts is shown. We collected white light transmission spectra for different values of the gate voltage V_g as shown in Figure 1(c). In this figure a transmittance minimum is observed at a wavelength of 622 nm. This is associated with the neutral exciton transition of the 1L-WS_2, labelled as X^o. In this figure we also observe the appearance of an asymmetric broadening associated with the weak transmittance of negatively charged excitons,[23] or negative trions, at a wavelength of 632 nm, which is labelled as X^-. We observe a weakening in the transmission minimum associated with the neutral excitons as we sweep the gate voltage from -5 V to +5 V. We also observed strengthening of the feature associated with the negative trions. To clarify this observation, we extract the change in transmission associated with X^o and X^- as a function of V_g. These data are shown in Figure 1(d) where values below one indicate how much the transmission is reduced in strength, whilst values above one indicate how much the transmission increases in strength. We observed no significant electrical current through the hBN barrier in this range of voltages (see supporting information Figure S5), which suggests that the free electrons are accumulated on the WS_2 which then leads to a reduction in the excitation rate of neutral excitons due to strong Coulomb repulsion between free carriers filling the conduction band.[24]

2.2. Tuneable microcavity

A tuneable microcavity was completed by adding a second silver mirror (top mirror) close to the top of the WS_2 transistor, as shown in Figure 2(b). For the microcavity we collected transmission spectra as a function of the thickness of the air gap between the hBN spacer and the top silver mirror in a region where there is no WS_2. These transmission spectra are then

compared to the modelled spectra from which we extract the experimental value for the thickness of the air gap (for details on modelling see the supporting information), as shown in the left panels of Figure 2(a). Here we identify the second-, third-, and fourth-order cavity modes. We observe excellent stability of our tuneable system, and very good quality of the microcavity modes compared to modelling. We repeated these measurements in a region of the microcavity where the 1L-WS_2 was present, keeping the gate voltage fixed at 0 V. These measurements were compared to the model and are shown in the right panels of Figure 2(a). Here we observe a splitting of the cavity modes at a wavelength of 622 nm, associated with the neutral exciton transition of WS_2. The mode splitting of the three cavity modes observed is greater than that of both the empty cavity mode and the exciton line widths (36 and 35 meV respectively), demonstrating that the system is in the strong coupling regime. We fit the calculated transmittance of a strongly coupled 1L-WS2-microcavity with an air gap of 787 nm, which corresponds to the third-order cavity mode, to the experimental observation as shown in Figure 2(c), where the free parameter was the oscillator strength of WS_2; we found that the best fit was achieved for an oscillator strength of $f = 2.6$. A comparison between the calculated and the measured transmittance spectra of a bare 1L-WS_2 is shown in Supporting Information Figure S3. The oscillator strength estimated in our experiments is significantly larger than values reported for WS_2 on SiO_2 or Al_2O_3 substrates.[12,21] The origin of this discrepancy could be the difference in the dielectric environment provided by the hBN flake in our devices, and also the fact that hBN provides an atomically smooth surface (roughness lower than 0.5 nm as measured by atomic force microscopy) which may reduce surface scattering and trapping effects in the WS_2/hBN interface.

2.3. Electrical control of the light-matter coupling

We next discuss the evolution of the cavity mode splitting in the strong coupling regime for different gate voltages ranging from -8 V to +8 V. To study the exciton and photon nature of the polariton bands we performed an analysis of the experimental data using a two coupled oscillator model, from which we obtained the Hopfield coefficients as described in the supporting information. We focused this analysis on the splitting of the third-order cavity mode, for four values of the gate voltage: -8 V, +3V, +5 V, and +6 V. These results are shown in Figure 3(a), in which the four values of the gate voltage are indicated. On each plot we show the position of the neutral exciton transition of WS_2 as a horizontal dashed line, and the third-order cavity mode as an oblique dashed line. The circles are the peak maxima obtained by fitting pseudo-Voigt functions to the experimental data for each value of the air gap. We then fit the coupled oscillator model to the position of the peak maxima. The input parameter in this analysis is the experimental value of the Rabi splitting, which corresponds to the transmission peak splitting at the point where the neutral exciton transition crosses the bare cavity mode. From the coupled oscillator model we find the Hopfield coefficients which we show in Figure 3(b) for the lower polariton band and (c) for the upper polariton band. We observe that the lower polariton band becomes more photon-like in nature for the most positive values of the gate voltage and therefore less excitonic in nature. The upper polariton band becomes more excitonic in nature for the most positive values of the gate voltage. The behavior of both of the polariton bands suggests a decoupling between excitons and cavity photons that occurs when a positive gate voltage is applied. A decoupling between excitons and cavity photons can also be observed as a reduction of the Rabi splitting as a function of the gate voltage as shown in Figure 4. In this figure we show the transmittance peak splitting for the (a) third-, (b) fourth-, and (c) fifth-order cavity modes as a function of gate voltage. These modes correspond to fixed air gaps of 787 ± 3 nm, 1097 ± 3 nm, and 1408 ± 3 nm respectively. For the three modes we observe a

dependence of the Rabi splitting on the gate voltage; the Rabi splitting reaches a saturation value when sufficiently negative voltages are applied to the transistor. In addition, the maximum splitting is lower for higher order cavity modes, as expected due to the weaker fields associated with the higher-order modes (see also supporting information Figure S6). From these measurements we obtain the Rabi splitting as a function of the gate voltage for the three cavity modes as shown in Figure 5(a). In this figure we also indicate the exciton line width, which is equal to or larger than any of the three cavity mode line widths, indicating that the system is in the strong coupling regime when the Rabi splitting is greater than the exciton line width.

2.4. Rabi splitting and density of free electrons

We now focus our attention on obtaining the dependence of the oscillator strength of WS_2 as we change the gate voltage, a dependence that we can relate to an increase of the density of free electrons in the WS_2. To do this we analyze the splitting of the third-order cavity mode. We first calculate the transmittance spectrum as shown in Figure 2(c) with an oscillator strength of $f_0 = 2.6$, which results in a Rabi splitting of 60 meV for the third-order mode at a gate voltage of 0 V. Prior to these measurements, we applied a sufficiently negative gate voltage to remove any excess of free electrons in WS_2, so f_0 is our initial oscillator strength for zero density of free electrons in the TMD. Next, we vary the oscillator strength in our calculations to reproduce the values of the Rabi splitting shown in Figure 5(a) for different values of the gate voltage. The density of free electrons N can be obtained by inserting the known values of the oscillator strength, f, in Equation (1),

$$f(N) = \frac{f_0}{1+\frac{N}{N_S}}, \tag{1}$$

where the saturation number N_s is defined as the number density of carriers at which the oscillator strength is reduced to a half of the initial value f_0. The value of can be estimated for

any 2-dimensional system that allows for the excitation of excitons and free carriers either in the conduction or the valence band. For our analysis we used , extracted from reference[25] where is the effective exciton-Bohr radius of WS_2, which has been taken from reference[26] to be a value of 2 nm corresponding to the X^0 exciton transition. These results are shown in Figure 5(b), where we also include the saturation function as described in Equation (1). The density of free electrons *N* found in this way agrees well with what is expected in a TMD system that behaves below the level of the Mott transition,[18,27] which has been estimated to occur at a density above 10^{13} cm^{-2}. In our system, we found the saturation density to be 9.6×10^{11} cm^{-2}, and in the range of voltages applied, the density of free electrons in the WS_2 ranges from 0 up to 3.2×10^{12} cm^{-2}.

3. Summary and conclusions

In summary, we studied continuous control over the light-matter coupling of exciton-polaritons in a WS_2 microcavity at room temperature. We achieved this by controlling the charge carrier density in the semiconductor material. Due to the Coulomb interaction the free carriers repel each other and screen the oscillator strength of excitons in WS_2. A specially designed WS_2 based field effect transistor was built on one of the mirrors of the microcavity,[16] then a second mirror was placed on top of the transistor leaving an air gap which we were able to control with a precision of ±3 nm in our tuneable system. This tuneability allowed us to study the polariton bands as a function of the thickness of the air gap, and we accessed different cavity modes ranging from the second-order to the fifth-order. For each of the cavity modes, at the resonance condition for WS_2 excitons forming exciton-polaritons, we were able to record transmittance spectra over a range of gate voltages, from -8 V to +8 V, observing a dependence of the Rabi splitting as a function of the gate voltage. Over this range of voltages, we calculated the variation of the oscillator strength in the TMD film, extracted from modelling the transmittance

spectra to match the measured values of the Rabi splitting. We attributed the change in the oscillator strength of WS_2 to Coulomb screening by the free electrons populating the conduction band of the TMD, we were then able to extract the density of free carriers in the conduction band, which ranges from 0 cm^{-2}, at a gate voltage of 0 V, up to $3.2\times10^{12}cm^{-2}$, for a gate voltage of +8 V. Over this range of density of free carriers, the Rabi splitting ranges from a maximum value, which depends on the cavity mode chosen, down to zero, so the system spans the strong to weak coupling regimes. This control of the Rabi splitting could also be extended to exciton-polaritons in p-type semiconductors with a strong excitonic resonance by injecting holes in the valence band of the material.

4. Experimental Section

Heterostructure: Flakes of WS_2 and hBN were prepared by micromechanical exfoliation of bulk single crystals, and WS_2/hBN heterostructures were assembled by a dry transfer method. Bulk WS_2 single crystals were purchased from HQgraphene, while bulk hBN single crystals were purchased from Manchester Nanomaterials. Flakes are initially mechanically exfoliated onto a polydimethylsiloxane (PDMS) film. The PDMS film with the hBN flake is then inverted and aligned with the target substrate, which is a silver coated quartz glass prepared by thermal evaporation. When the hBN flake is stuck on the target substrate (by heating the substrate to T = 60ºC), the polymer is slowly brought back and the hBN flake remains on the silver film. This process is repeated in order to place the WS_2 flake on top of hBN. Monolayer flakes of WS_2 display a bright and narrow linewidth emission at room temperature (~40 meV) consistent with other works based on the highest quality WS_2 films.[12,13] The hBN used was also characterized previously[28] using graphene Hall bars to understand the impurities. It was found that graphene Hall bars display charge carrier mobilities as high as 50,000 $cm^2V^{-1}s^{-1}$ at room temperature at charge concentrations of 5×10^{11} cm^{-2}. This value is comparable to literature

values for devices based on the highest quality hBN crystals. Breakdown voltages of our source hBN are also consistent with high quality hBN at 0.8-1 Vnm^{-1} indicating again the high quality of the dielectric. The leakage current in all gating measurements in our study was recorded and was always $<10^{-9}$ A (see supplementary information Figure S5).

Tuneable microcavity setup: The tuneable microcavity was completed by a top mirror placed on a piezo-electric stage (Thorlabs® MAX313D) controlled externally (Thorlabs® MDT30B) through LabView®. Both mirrors had five degrees of freedom; three translational and two rotational. The alignment procedure to make both of the mirrors parallel consisted of sending red light by using a band pass filter in front of the white light source. We then examined the transmitted light on a digital camera. The transmitted light consisted of an interference pattern of rings. By rotating the top mirror we adjusted the ring pattern until we reached the center of the pattern. The accuracy of this procedure depends on the magnification of the optical system, which in turn determined how many lines of the ring pattern could be observed on the computer screen, the accuracy also depended on the quality of the microcavity and the line-width of the band-pass filter, which determined the width of the lines that form the rings pattern.

Optical and electrical measurements: Transmission measurements were performed in a confocal setup. The light source (Thorlabs® SLS201L/M) was fiber coupled, collimated and focused by X10 objective lenses through the bottom mirror. To collect the transmitted light through the top mirror a X50 objective lens was used (Olympus® SLMPLN50X), which was then focused on a fiber coupled spectrometer (OceanOptics® Flame). The gate voltage was applied by a Keithley® 2450 SMU; gate voltage and tunneling current were recorded for the different values of the cavity length. The top mirror was placed on a piezo-stage (Thorlabs® MAX312D, MDT630B) which allows for a control of the cavity length with a precision of 3

nm. Transmittance, piezo-stage voltage, and gate voltage measurements were synchronized using LabView®.

Supporting Information
Supporting Information is available from the Wiley Online Library or from the author.

Acknowledgements

The authors acknowledge Prof. Misha Portnoy for several insightful discussions. HF, and WLB thank Dr. Lucas Flatten for his advice on the tuneable microcavity setup. The authors also acknowledge financial support from the Engineering and Physical Sciences Research Council (EPSRC) of the United Kingdom, via the EPSRC Centre for Doctoral Training in Metamaterials (Grant No. EP/L015331/1). FW acknowledges support from the Royal Academy of Engineering. SR acknowledges financial support from The Leverhulme Trust research grants "Quantum Drums" and "Quantum Revolution". WLB acknowledges the support of the European Research Council through the project Photmat (ERC-2016-ADG-742222: www.photmat.eu).

Received: ((will be filled in by the editorial staff))
Revised: ((will be filled in by the editorial staff))
Published online: ((will be filled in by the editorial staff))

References

[1] J. Kasprzak, M. Richard, S. Kundermann, A. Baas, P. Jeambrun, J. M. J. J. Keeling, F. M. Marchetti, M. H. Szymańska, R. André, J. L. Staehli, V. Savona, P. B. Littlewood, B. Deveaud, L. S. Dang, M. H. Szymánska, R. André, J. L. Staehli, V. Savona, P. B. Littlewood, B. Deveaud, L. S. Dang, *Nature* **2006**, *443*, 409.

[2] A. Amo, D. Sanvitto, F. P. Laussy, D. Ballarini, E. Del Valle, M. D. Martin, A. Lemaître, J. Bloch, D. N. Krizhanovskii, M. S. Skolnick, C. Tejedor, L. Viña, *Nature*

2009, *457*, 291.

[3] A. Amo, J. Lefrère, S. Pigeon, C. Adrados, C. Ciuti, I. Carusotto, R. Houdré, E. Giacobino, A. Bramati, *Nat. Phys.* **2009**, *5*, 805.

[4] G. Lerario, A. Fieramosca, F. Barachati, D. Ballarini, K. S. Daskalakis, L. Dominici, M. De Giorgi, S. A. Maier, G. Gigli, S. Kéna-Cohen, D. Sanvitto, *Nat. Phys.* **2017**, *13*, 837.

[5] T. Karzig, C.-E. Bardyn, N. H. Lindner, G. Refael, *Phys. Rev. X* **2015**, *5*, 031001.

[6] Q.-Y. Liang, A. V Venkatramani, S. H. Cantu, T. L. Nicholson, M. J. Gullans, A. V Gorshkov, J. D. Thompson, C. Chin, M. D. Lukin, V. Vuletić, *Science (80-.).* **2018**, *359*, 783.

[7] A. Reiserer, G. Rempe, *Rev. Mod. Phys.* **2015**, *87*, 1379.

[8] T. Mueller, E. Malic, *npj 2D Mater. Appl.* **2018**, *2*, 29.

[9] T. C. Berkelbach, M. S. Hybertsen, D. R. Reichman, *Phys. Rev. B* **2013**, *88*, 045318.

[10] X. Liu, T. Galfsky, Z. Sun, F. Xia, E. Lin, Y.-H. Lee, S. Kéna-Cohen, V. M. Menon, *Nat. Photonics* **2015**, *9*, 30.

[11] S. Dufferwiel, S. Schwarz, F. Withers, A. A. P. Trichet, F. Li, M. Sich, O. Del Pozo-Zamudio, C. Clark, A. Nalitov, D. D. Solnyshkov, G. Malpuech, K. S. Novoselov, J. M. Smith, M. S. Skolnick, D. N. Krizhanovskii, A. I. Tartakovskii, *Nat. Commun.* **2015**, *6*, 8579.

[12] S. Wang, S. Li, T. Chervy, A. Shalabney, S. Azzini, E. Orgiu, J. A. Hutchison, C. Genet, P. Samorì, T. W. Ebbesen, *Nano Lett.* **2016**, *16*, 4368.

[13] L. C. Flatten, Z. He, D. M. Coles, A. A. P. Trichet, A. W. Powell, R. A. Taylor, J. H. Warner, J. M. Smith, *Sci. Rep.* **2016**, *6*, 33134.

[14] T. Chervy, S. Azzini, E. Lorchat, S. Wang, Y. Gorodetski, J. A. Hutchison, S. Berciaud, T. W. Ebbesen, C. Genet, *ACS Photonics* **2018**, *5*, 1281.

[15] S. Dufferwiel, T. P. Lyons, D. D. Solnyshkov, A. A. P. Trichet, A. Catanzaro, F.

Withers, G. Malpuech, J. M. Smith, K. S. Novoselov, M. S. Skolnick, D. N. Krizhanovskii, A. I. Tartakovskii, *Nat. Commun.* **2018**, *9*, 4797.

[16] H. Fernandez, S. Russo, W. L. Barnes, in *2017 Conf. Lasers Electro-Optics Eur. Eur. Quantum Electron. Conf.*, IEEE, **2017**, pp. 1–1.

[17] Y. Li, A. Chernikov, X. Zhang, A. Rigosi, H. M. Hill, A. M. van der Zande, D. A. Chenet, E.-M. Shih, J. Hone, T. F. Heinz, *Phys. Rev. B* **2014**, *90*, 205422.

[18] A. Chernikov, A. M. Van Der Zande, H. M. Hill, A. F. Rigosi, A. Velauthapillai, J. Hone, T. F. Heinz, *Phys. Rev. Lett.* **2015**, *115*, 126802.

[19] R. Houdré, J. L. Gibernon, P. Pellandini, R. P. Stanley, U. Oesterle, C. Weisbuch, J. O'Gorman, B. Roycroft, M. Ilegems, *Phys. Rev. B* **1995**, *52*, 7810.

[20] W. Gao, X. Li, M. Bamba, J. Kono, *Nat. Photonics* **2018**, *12*, 362.

[21] B. Chakraborty, J. Gu, Z. Sun, M. Khatoniar, R. Bushati, A. L. Boehmke, R. Koots, V. M. Menon, *Nano Lett.* **2018**, *18*, 6455.

[22] K. Zhang, Y. Feng, F. Wang, Z. Yang, J. Wang, *J. Mater. Chem. C* **2017**, *5*, 11992.

[23] J. Shang, X. Shen, C. Cong, N. Peimyoo, B. Cao, M. Eginligil, T. Yu, *ACS Nano* **2015**, *9*, 647.

[24] B. Zhu, X. Chen, X. Cui, *Sci. Rep.* **2015**, *5*, 9218.

[25] S. Schmitt-Rink, D. S. Chemla, D. A. B. Miller, *Phys. Rev. B* **1985**, *32*, 6601.

[26] Z. Ye, T. Cao, K. O'Brien, H. Zhu, X. Yin, Y. Wang, S. G. Louie, X. Zhang, *Nature* **2014**, *513*, 214.

[27] A. Chernikov, C. Ruppert, H. M. Hill, A. F. Rigosi, T. F. Heinz, *Nat. Photonics* **2015**, *9*, 466.

[28] A. De Sanctis, J. D. Mehew, S. Alkhalifa, F. Withers, M. F. Craciun, S. Russo, *Nano Lett.* **2018**, *18*, 7919.

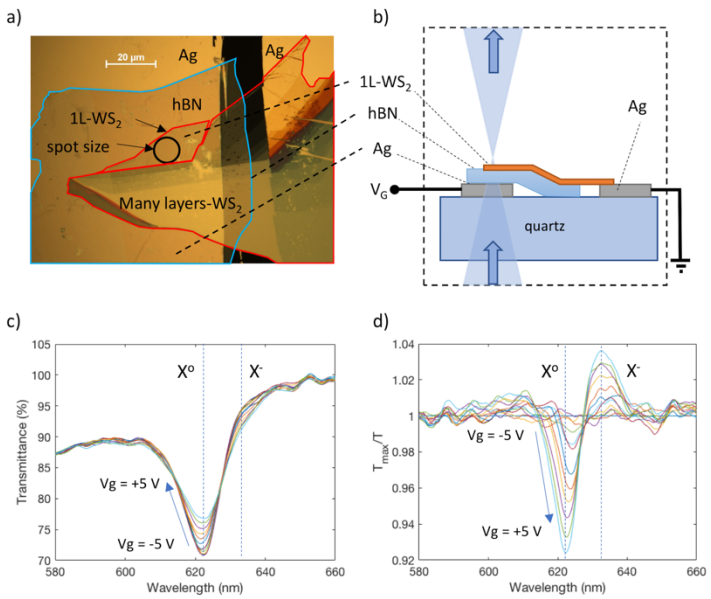

Figure 1. (a) Top view microscope image of the WS_2/hBN/Ag heterostructure on quartz. Color lines indicate flake edges: blue for hBN, and red for WS_2. (b) Schematic cross section of the WS_2-based transistor. Arrows indicate the propagation direction of the white light. (c) White light transmittance of the 1L-WS_2 for different gate voltages from -5 V to +5 V. The positions of neutral excitons X^0 and negatively charged excitons, or negative trions X^-, are indicated. (d) Data shown in (c) normalized to the transmittance spectrum for V_g = -5 V, which is the reference T_{max}. This plot shows how the transmission for both the neutral excitons and the negative trions change for the different values of gate voltage.

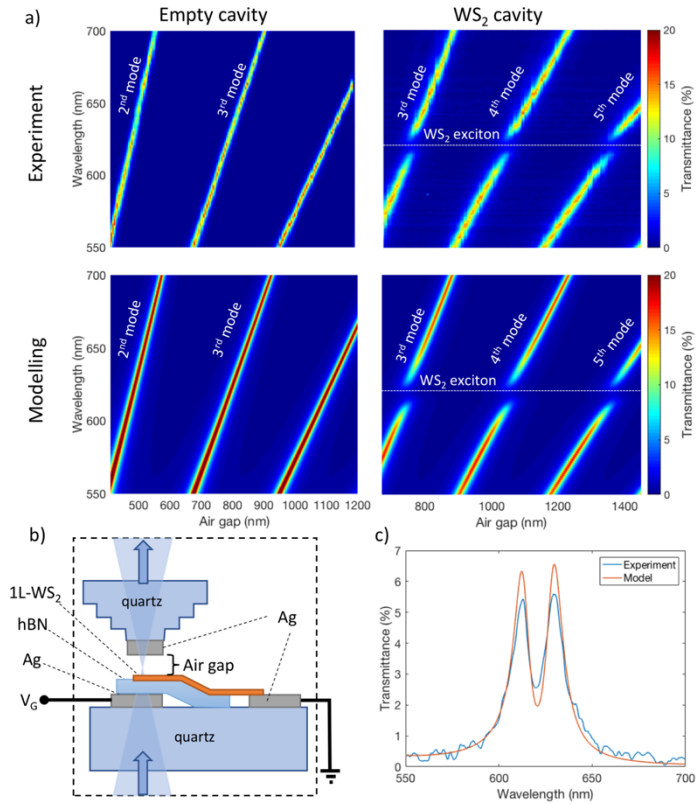

Figure 2. (a) Experimental data and modelling of the empty cavity modes and the WS_2-cavity modes as a function of the air gap between the WS_2 flake and the top silver mirror. (b) Schematic of the tuneable microcavity, which consists of the same sample shown in Figure 1(b) but with a top mirror added leaving a small gap between the bottom and top mirrors. (c) Experimental and calculated transmittance of a strongly coupled WS_2 microcavity. Strong coupling was achieved for a cavity air gap of 787 ± 3 nm, which corresponds to the third-order cavity mode.

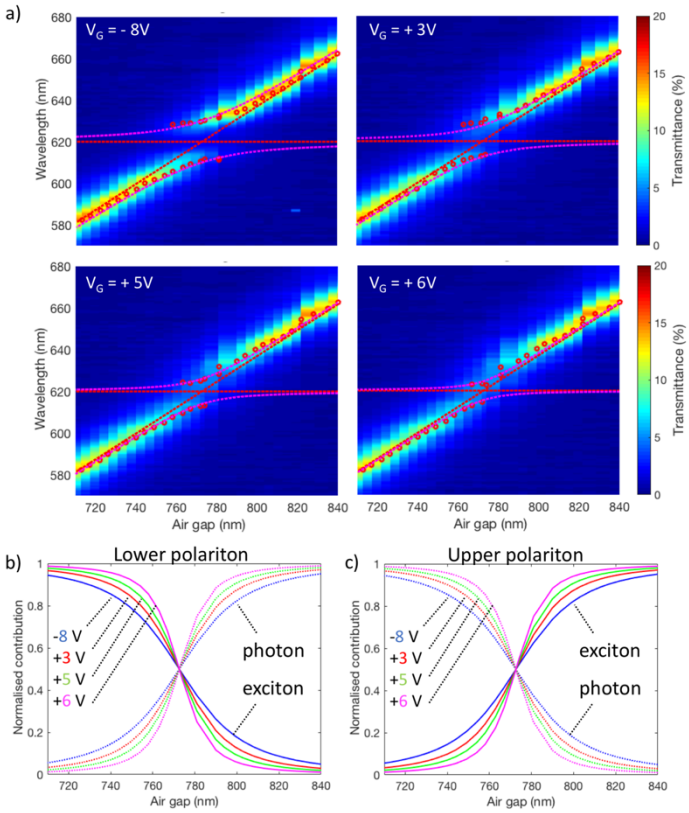

Figure 3. (a) Analysis of the transmittance spectra of the third-order cavity mode of the WS_2 microcavity for different values of the gate voltage. Dashed oblique lines are the uncoupled cavity modes obtained from modelling an empty microcavity (see Figure 2(a)), horizontal dashed lines indicate the neutral exciton transition of WS_2, and curved dashed lines are the lower and upper polariton bands obtained from the coupled oscillator model. Circles are the experimental peak center of the transmission data. (b), and (c) are the Hopfield coefficients of the lower and upper polariton bands respectively. The different colors correspond to different values of the gate voltage. Continuous lines correspond to the exciton contribution to the polariton bands. Dashed lines correspond to the cavity photon contribution.

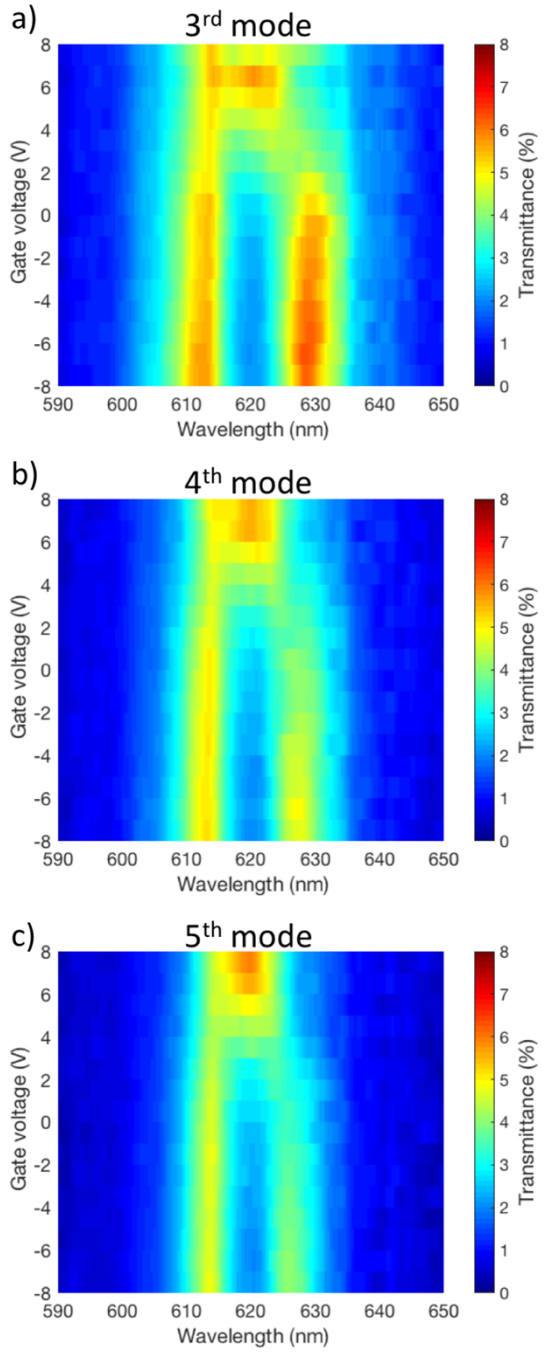

Figure 4. Transmittance spectra of a WS_2 microcavity for different values of the gate voltage and for a fixed air gap: (a) 787 ± 3 nm, (b) 1097 ± 3 nm, and (c) 1408 ± 3 nm, which correspond to the third-, fourth- and fifth-order cavity modes respectively.

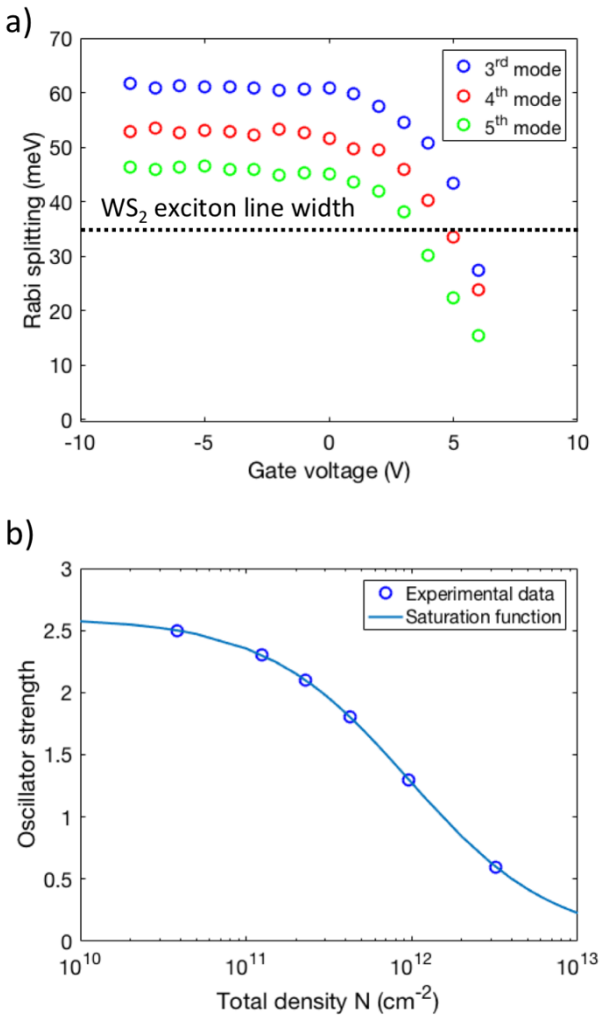

Figure 5. (a) Rabi splitting as a function of the gate voltage obtained from the data shown in Figure 4. The three different cavity modes are shown as different colors: blue for the 3rd mode, red for the 4th mode, and green for the 5th mode. (b) Oscillator strength as a function of the total density of electrons *N*. The saturation function (Equation (1)) is also shown.

Electrical control of exciton-polaritons at room temperature is demonstrated in a WS_2-based field effect transistor embedded in a tuneable optical microcavity. The application of a gate voltage increases the density of free charge carriers in the WS_2 monolayer. Coulomb repulsion of the injected carriers screens the oscillator strength of WS_2 excitons reducing the Rabi splitting of exciton-polaritons.

Keyword exciton-polaritons

H. A. Fernandez, F. Withers, S. Russo, W. L. Barnes*

Electrically tuneable exciton-polaritons through free electron doping in monolayer WS_2 microcavities

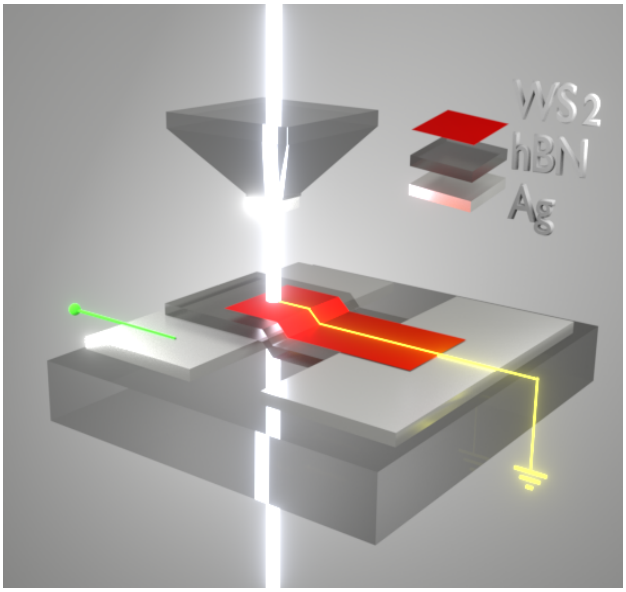

Supporting Information

Electrically tuneable exciton-polaritons through free electron doping in monolayer WS_2 microcavities

*Henry A. Fernandez, Freddie Withers, Saverio Russo, and William L. Barnes**

1. Tuneable microcavity design

Figure S1 shows the calculated electric field in the microcavity used in experiments for a fixed cavity length and for a single wavelength, to be 622 nm. Figure S1(a) shows the electric field map where the interfaces of the different materials are indicated as vertical white lines. This considers an air gap of 787 nm, for which it is possible to observe strong coupling as confirmed by our measurements (see main text, Figure 2(c)). This simulation also considers the known thickness of the different materials: 40 nm for silver, 46 nm for hBN, and 0.7 nm for WS_2.[1] The optical parameters used in simulations are described in the Numerical calculations section in this supporting information. We observe in Figure S1(a) the splitting of the third-order cavity mode, which gives a Rabi splitting of 60 meV. We also show the real part of the complex refractive index of the different materials in Figure S1(b).

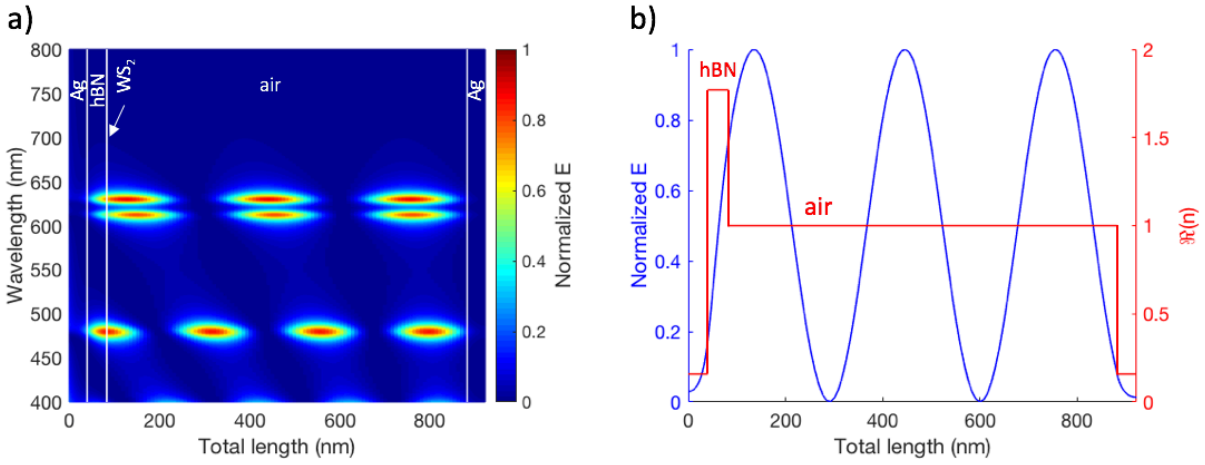

Figure S1. Calculations of the electric field in the microcavity structure. (a) is a map of the electric field for a microcavity with an air gap of 787 nm, for which the third cavity mode is observed to be split in two, signature of the strong coupling regime. The blue line in (b) is the electric field profile for a wavelength of 622 nm, which correspond to the neutral exciton transition of 1L-WS_2. The red lines are the values of the real part of the refractive index of the

different materials in the microcavity structure. The total length is the sum of the thicknesses of the silver films, and the hBN flake (measured by AFM), and the air gap.

In Figure S2 we show the AFM measurements of the edge of the hBN flake on silver. Figure S2(a) is a top view and (b) is a 3-dimensional representation of (a). From these measurements we determined the hBN thickness to be 46 ± 1 nm, and the surface roughness of silver and hBN, to be 1 ± 0.1 nm and 0.2 ± 0.05 nm respectively.

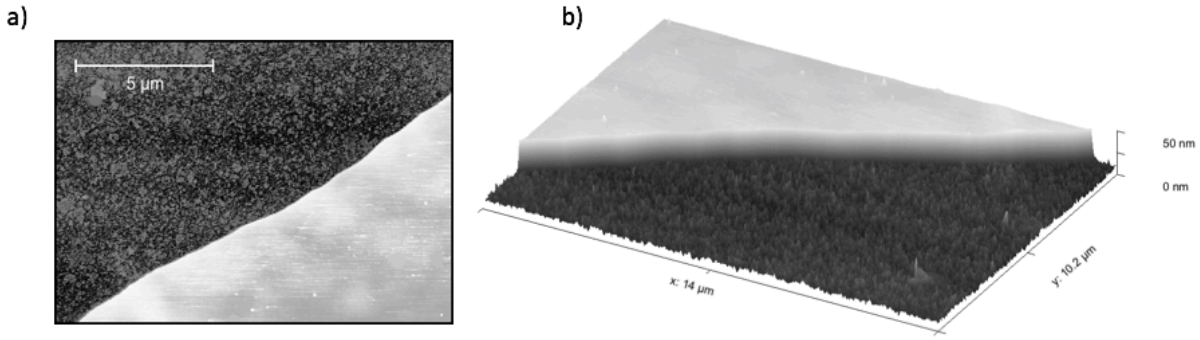

Figure S2. AFM images of an edge of the hBN flake on silver. (b) is a 3-dimensional representation of (a). From this data we measured a hBN thickness of 46 ± 1 nm, and a RMS surface roughness of 0.2 ± 0.05 nm.

2. Properties of WS_2

In Figure S3 we show the experimental and calculated transmittance of a bare WS_2 monolayer. For the calculations we used the optical parameters as described in the Numerical calculations section in this supporting information.

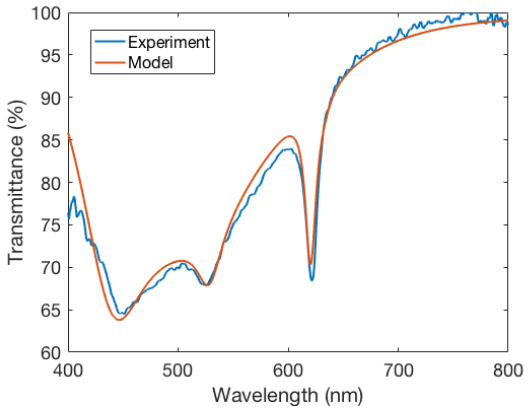

Figure S3. Experimental transmittance of a WS_2 monolayer and the calculated transmittance using parameters listed in Table S1.

In Figure S4 we show the transmittance of the WS_2 monolayer for different values of the gate voltage. This is the same data shown in the main text in Figure 1(c), but here it is extended to a wavelength of 400 nm. The transmittance minimum at 525 nm is associated with the B exciton transition of WS_2, which does not change as we sweep the gate voltage from -5 V to +5 V.

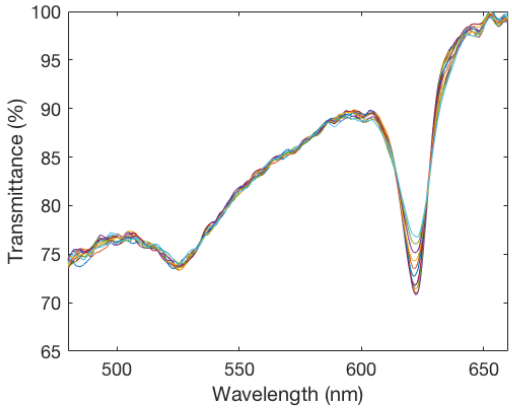

Figure S4. Same measurements shown in the main text in Figure 1(c) but extended to shorter wavelengths to show the transmittance dip associated with the B exciton transition of WS_2 at a wavelength of 525 nm. We observe no change in the B exciton, and a significant change in the X^0 exciton at 622 nm as we apply a gate voltage.

3. I-V curves

In Figure S5 we show I-V characteristic for the WS_2/hBN/Ag stack. These are consecutive measurements for all the different cavity lengths, ranging from 700 nm up to 1450 nm. Over this range we observe no significant change in the I-V characteristic.

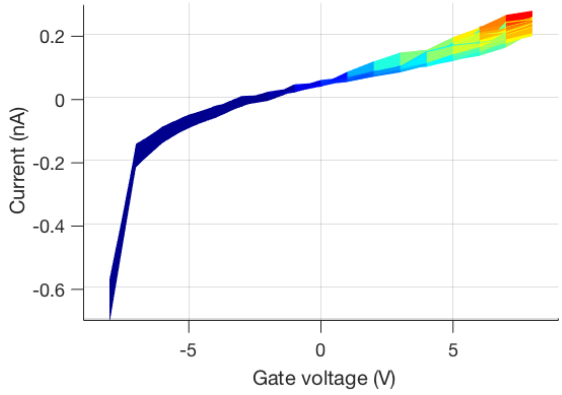

Figure S5. Superposition of consecutive measurements of the I-V characteristic of the WS_2-based transistor embedded in the microcavity for all the cavity lengths from third- to fifth-order cavity modes.

4. Rabi splitting and cavity modes

In Figure S6 we show the measured and calculated maximum values of the Rabi splitting as a function of the cavity mode. We observe a very good agreement between the two sets of data. We also observe that in optimum conditions, the Rabi splitting can reach a value of 98 meV. To the best of our knowledge, such large value of the Rabi splitting in a TMD-microcavity structure has not previously been achieved experimentally at room temperature. This large value of the Rabi splitting can be achieved due to the excellent conditions the hBN flake provide for an efficient coupling of WS_2 excitons to cavity modes, and also due to the large oscillator strength of exfoliated WS_2 flakes, after removing any excess of free electrons.

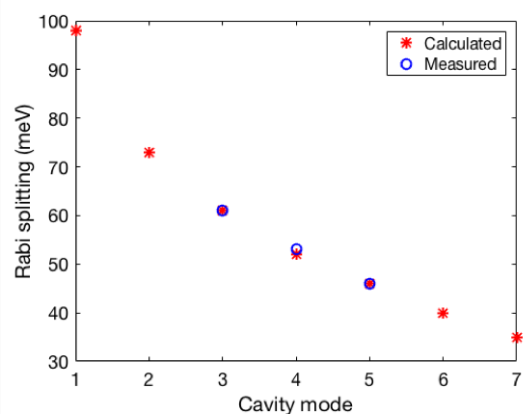

Figure S6. Calculated and measured maximum Rabi splitting as a function of the order of the cavity modes.

5. Numerical calculations

5.1 Transmission spectra

To compare the measured transmittance of the microcavity with the calculated spectra, we modelled the electric field (see Figure S1) and the transmittance of the multilayer structure using a Fresnel formulation.[2] The input parameters in this formulation are the thickness and the complex permittivity of the different layers in the microcavity. The complex permittivity of silver and WS_2 are shown in Equations (S1) and (S2), respectively,

$$\epsilon_{Ag}(E) = 1 - \frac{f_0 \hbar\omega_p^2}{E^2 - i\Gamma_0 E} + \sum_{j=1}^{3} \frac{f_j \hbar\omega_p^2}{E_j^2 - E^2 - i\Gamma_j E} \quad \text{(S1)}$$

$$\epsilon_{WS_2}(E) = \epsilon_\infty + \sum_{j=1}^{3} \frac{f_j \hbar\omega_0^2}{E_j^2 - E^2 - i\Gamma_j E} \ . \quad \text{(S2)}$$

In Equation (S1), f_0 is the oscillator strength of the intraband transition with damping factor Γ_0, and ω_p is the plasma frequency of silver. $f_0 = 0.845$, $\Gamma_0 = 0.048\ eV$, and $\hbar\omega_p = 9.010\ eV$.[3] In Equation (S2), $\epsilon_\infty = 1$, is the background permittivity of WS_2, and ω_0 is such that $\hbar\omega_0 = 1\ eV$. The other parameters used for calculations are listed in Table S1.[3] For WS_2 we obtained the listed values in Table S1 from fitting the calculated transmission spectrum to the measured transmission of a WS_2 monolayer, as shown in Figure S3.

Table S1. Parameters for the calculation of the permittivities of silver and WS_2.

Material	f_1	f_2	f_3	$E_1(eV)$	$E_2(eV)$	$E_3(eV)$	$\Gamma_1(eV)$	$\Gamma_2(eV)$	$\Gamma_3(eV)$
Silver	0.065	0.124	0.011	0.816	4.481	8.185	3.886	0.452	0.065
WS_2	2.600	0.100	4.500	2.008	1.962	2.380	0.035	0.040	0.200

5.2 Exciton and photon nature of exciton-polaritons

To quantitatively study the exciton and photon nature of exciton-polaritons in our microcavity structure, we calculated the exciton-polariton bands using a coupled oscillator model (equation (S3)). This model consists of a representation of microcavity photons and WS_2 excitons as coupled oscillators that exchange energy at a rate that is described by the coupling strength Ω, which for the case of exciton-polaritons corresponds to the Rabi splitting. The coupled oscillator model has been modified such that the microcavity modes, E_{cav}, are functions of the cavity length for a fixed wavevector normal to the microcavity plane.[4] Exciton modes, E_{ex}, are constant values. The coupled oscillator model can be represented in matrix form as follows:

$$\begin{pmatrix} E_{cav} - E_{L,U} & \Omega/2 \\ \Omega/2 & E_{ex} - E_{L,U} \end{pmatrix} \begin{pmatrix} a_{L,U} \\ b_{L,U} \end{pmatrix} = 0, \quad \text{(S3)}$$

where $E_{L,U}$ are the eigenvalues of the matrix that correspond to the lower (L) and upper (U) polariton bands, and the coefficients $a_{L,U}$ and $b_{L,U}$ comprise the eigenvectors of the matrix and obey the relation $|a_{L,U}|^2 + |b_{L,U}|^2 = 1$. The quantities $|a_{L,U}|^2$ and $|b_{L,U}|^2$ correspond to the Hopfield coefficients: they represent the fraction of photons and excitons that comprise each of the polariton bands.[5]

[1] S. Wang, S. Li, T. Chervy, A. Shalabney, S. Azzini, E. Orgiu, J.A. Hutchison, C. Genet, P. Samori, T.W. Ebbesen, *Nano Lett.* **2016**, 16, 4368.

[2] F.L. Pedrotti, L.M. Pedrotti, L.S. and Pedrotti, *Introduction to Optics*, Cambridge University Press, **2017**.

[3] A.D. Rakić, A.B. Djurišic, J.M. Elazar, and M.L. Majewski, *Appl. Opt.* **1998**, 37, 5271.

[4] L.C. Flatten, Z. He, D.M. Coles, A.A.P. Trichet, A.W. Powell, R.A. Taylor, J.H. Warner, J.M. Smith, *Sci. Rep.* **2016**, 6, 33134.

[5] J.J. Hopfield, *Phys. Rev.* **1958**, 112, 1555-1567.